ACS NANO
Cite This: ACS Nano 2017, 11, 11574-11583
www.acsnano.org

ARTICLE

Electronic Structure Reconfiguration toward Pyrite NiS_2 *via* Engineered Heteroatom Defect Boosting Overall Water Splitting

Hengjie Liu,[†] Qun He,[†] Hongliang Jiang,*[,†] Yunxiang Lin,[†] Youkui Zhang,[†,‡] Muhammad Habib,[†] Shuangming Chen,[†] and Li Song*[,†]

[†]National Synchrotron Radiation Laboratory, CAS Center for Excellence in Nanoscience, University of Science and Technology of China, Hefei, Anhui 230029, China

[‡]School of National Defense Science and Technology, Southwest University of Science and Technology, Mianyang, Sichuan 621010, China

Supporting Information

ABSTRACT: **Developing highly active and low-cost heterogeneous catalysts toward overall electrochemical water splitting is extremely desirable but still a challenge. Herein, we report pyrite NiS_2 nanosheets doped with vanadium heteroatoms as bifunctional electrode materials for both hydrogen- and oxygen-evolution reaction (HER and OER). Notably, the electronic structure reconfiguration of pyrite NiS_2 is observed from typical semiconductive characteristics to metallic characteristics by engineering vanadium (V) displacement defect, which is confirmed by both experimental temperature-dependent resistivity and theoretical density functional theory calculations. Furthermore, elaborate X-ray absorption spectroscopy measurements reveal that electronic structure reconfiguration of NiS_2 is rooted in electron transfer from doped V to Ni sites, consequently enabling Ni sites to gain more electrons. The metallic V-doped NiS_2 nanosheets exhibit extraordinary electrocatalytic performance with overpotentials of about 290 mV for OER and about 110 mV for HER at 10 mA cm^{-2} with long-term stability in 1 M KOH solutions, representing one of the best non-noble-metal bifunctional electrocatalysts to date. This work provides insights into electronic structure engineering from well-designed atomic defect metal sulfide.**

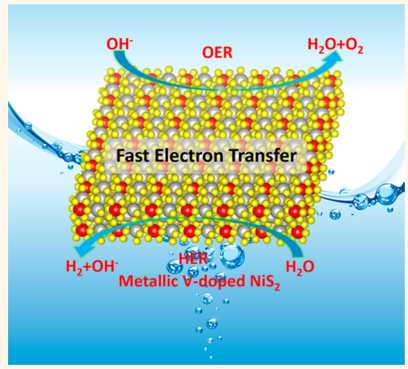

KEYWORDS: *electronic structure, defect engineering, X-ray absorption spectroscopy, metallic characteristics, water splitting*

Electrochemical water splitting as a promising way to continuously produce hydrogen has already attracted copious attention.[1−7] Despite the excellent catalytic performance of precious metal-based materials (RuO_2, IrO_2, Pt/C, *etc.*) for oxygen evolution reaction (OER) or hydrogen evolution reaction (HER),[8−10] the high price, deactivation, and low abundance substantially limit their large-scale applications.[11] As a consequence, extensive interest has been devoted to exploring nonprecious electrocatalysts with high catalytic performance toward both OER and HER.[12−19] Nevertheless, on account of entirely different reaction kinetics and proton-coupled electron-transfer processes, it still remains a grand challenge to construct efficient bifunctional electrocatalysts for achieving OER and HER simultaneously.[20−22] By means of serious investigations into extensive studies, desirable water splitting electrocatalysts are usually obtained by precise electronic structure regulation and active component integration.[23−27] For instance, electronic structure regulation of metallic 1T-MoS_2 was successfully conducted *via* interfacial charge polarization between single-walled carbon nanotubes (SWCNT) and 1T-MoS_2.[28] Furthermore, integration of 1T-MoS_2 (being active toward HER) and amorphous nickel−cobalt complexes (being active toward OER) exhibited high efficiency and robust performance toward overall electrochemical water splitting.[29]

Among these catalysts, nickel-based materials gain considerable attention owing to their earth-abundant reserves and low environmental toxicities as well as unique eight electrons in the 3d electron orbital which contributes to facile electronic structure regulation. Considering structure designs and mechanism explorations of nickel-based catalysts toward electrochemical water splitting, it could be concluded that nickel-based catalysts with semiconductor or insulator characteristics are generally unsatisfactory for the overall electrochemical water splitting process due to inherently poor electron transportation ability. Comparably, intrinsic metallic Ni_3N,

Received: September 13, 2017
Accepted: November 13, 2017
Published: November 13, 2017

DOI: 10.1021/acsnano.7b06501
ACS Nano 2017, 11, 11574−11583

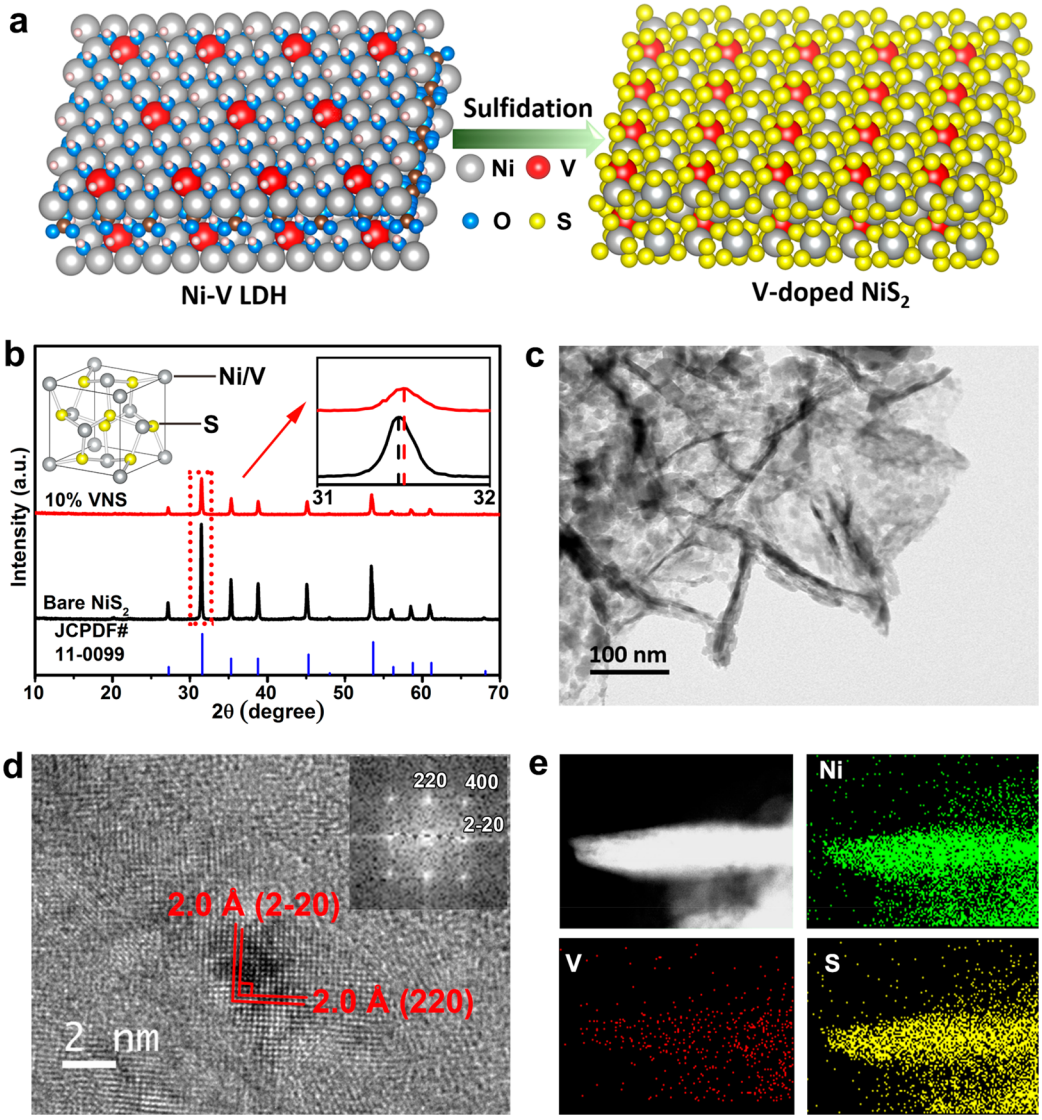

Figure 1. (a) Schematic illustration of the synthesis process for V-doped NiS_2. (b) PXRD patterns of bare NiS_2 and 10% VNS (inset: zoomed-in view of XRD patterns). (c, d) TEM images of 10% VNS. (e) HAADF image of 10% VNS and corresponding elements mapping image.

Ni_2P and Ni_3S_2 have been found to show excellent activities toward OER or HER.[30−35] Thus, realizing semiconductor-metal transitions via electronic structure engineering might be a promising strategy to optimize electrocatalytic performance.

Atomic defect engineering is considered an efficient approach to tune atomic structure of host materials and then realize electronic structure regulation.[36,37] According to previous reports, layered double hydroxides (LDHs) are generally composed of brucite-like layers with parts of the bivalent metal cations (M^{2+}) octahedrally coordinated by hydroxide ion being isomorphously replaced by the trivalent metal cations (M^{3+}), in which these metal cations are atomically dispersed and tunable within wide ranage.[38,39] Herein, pyrite nickel sulfide (NiS_2), one of typical narrow bandgap semiconductors, was employed as a proof-of-concept object. In order to better achieve highly homogeneous heteroatom displacement defect, we selected nickel hydroxide/nickel-vanadium LDH (NiV LDH) nanosheets as construct precursors, followed by facile sulfidation treatment to obtain NiS_2 and V-doped NiS_2. Specially, comprehensive insights provided by elaborate experiment investigations and density functional theory (DFT) calculations revealed that electronic structure of pyrite NiS_2 was reconfigured from typical semiconductive characteristics to metallic characteristics, and subsequently enhanced catalytic performance was delivered.

RESULTS AND DISCUSSION

Typically, NiS_2 and V-doped NiS_2 were prepared *via* employing gas-phase sulfidation onto nickel hydroxide/NiV LDH, as schematically illustrated in Figure 1a (bare NiS_2 in Figure S1). Briefly, nickel hydroxide/NiV LDH were first synthesized as precursors by a modified hydrothermal method (The XRD patterns were shown in Figure S2),[40] and then the target objects were obtained *via* facile sulfidation process (see Experimental Section for details). For simplicity, the NiS_2 and V-doped NiS_2 with 10% V molar doping (as summarized in Table S1) were marked as bare NiS_2 and 10% VNS, respectively. First, the powder X-ray diffraction (PXRD) patterns of the bare NiS_2 and 10% VNS were measured to investigate their crystal structures (Figure 1b). The PXRD pattern of bare NiS_2 matched well with the pyrite NiS_2 (JCPDF 11-0099). Specially, no distinct new peak could be observed

DOI: 10.1021/acsnano.7b06501
ACS Nano 2017, 11, 11574−11583

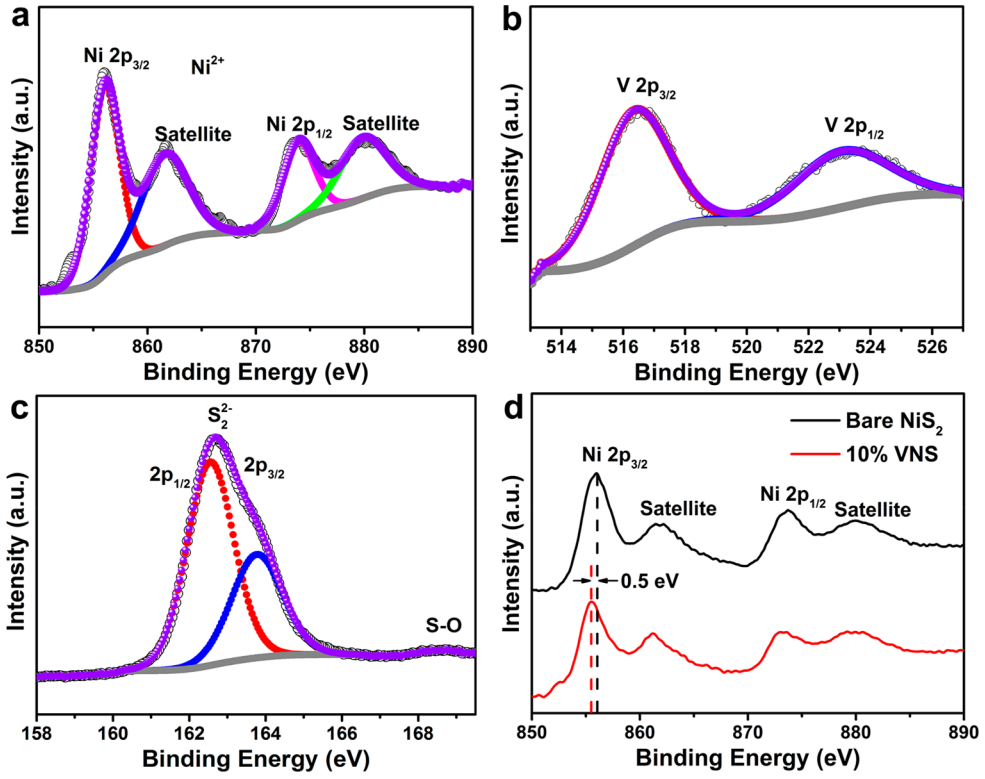

Figure 2. (a–c) High-resolution XPS of Ni 2p (a), V 2p (b), and S 2p (c). (d) Ni 2p XPS comparison of bare NiS_2 and 10% VNS.

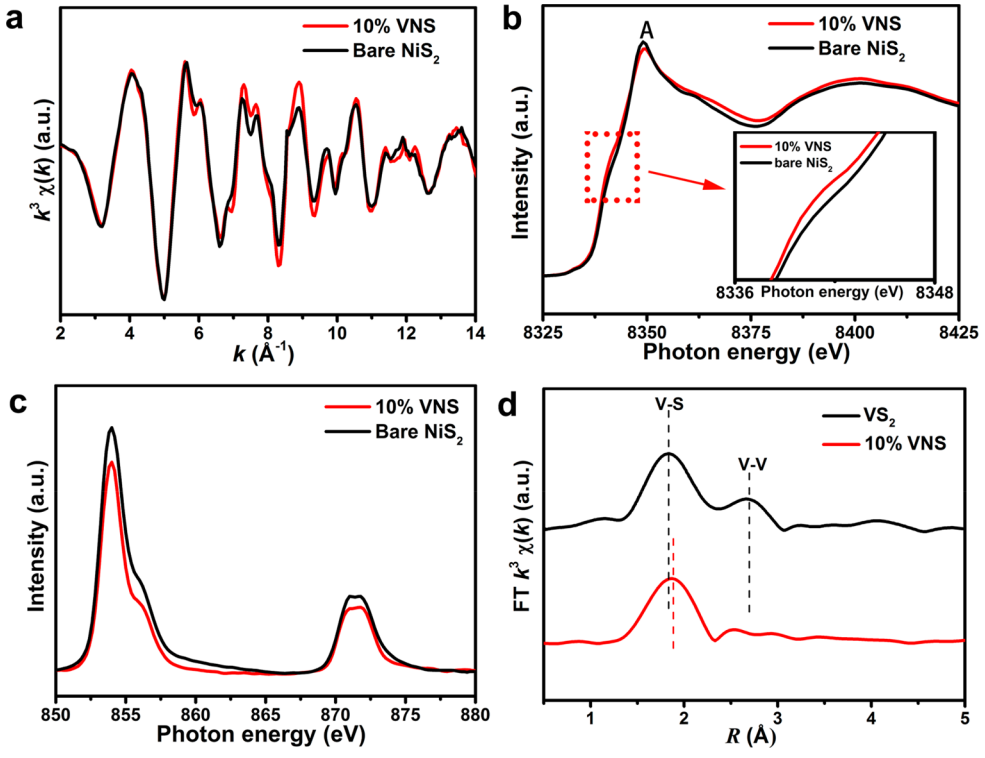

Figure 3. (a) Ni K-edge XAFS $k^3(\chi(k))$ oscillation curves of bare NiS_2 and 10% VNS. (b) Ni K-edge XANES of bare NiS_2 and 10% VNS (inset: zoomed-in view of the Ni K-edge XANES). (c) Ni L-edge XANES of bare NiS_2 and 10% VNS. (d) FT V K-edge FT($k^3(\chi(k))$) of VS_2 and 10% VNS.

after 10% V doping into the NiS_2, indicating the preservation of typical pyrite NiS_2. However, as shown in the inset of Figure 1b, the diffraction peaks of 10% VNS slightly shifted to a high angle direction compared to that of bare NiS_2, which illustrates decreased lattice parameter in doped NiS_2. This phenomenon was probably caused by V atoms substitution within Ni sites due to the different atom radius between the nickel atom and the doped vanadium atom. Morphology investigations (Figures

DOI: 10.1021/acsnano.7b06501
ACS Nano 2017, 11, 11574–11583

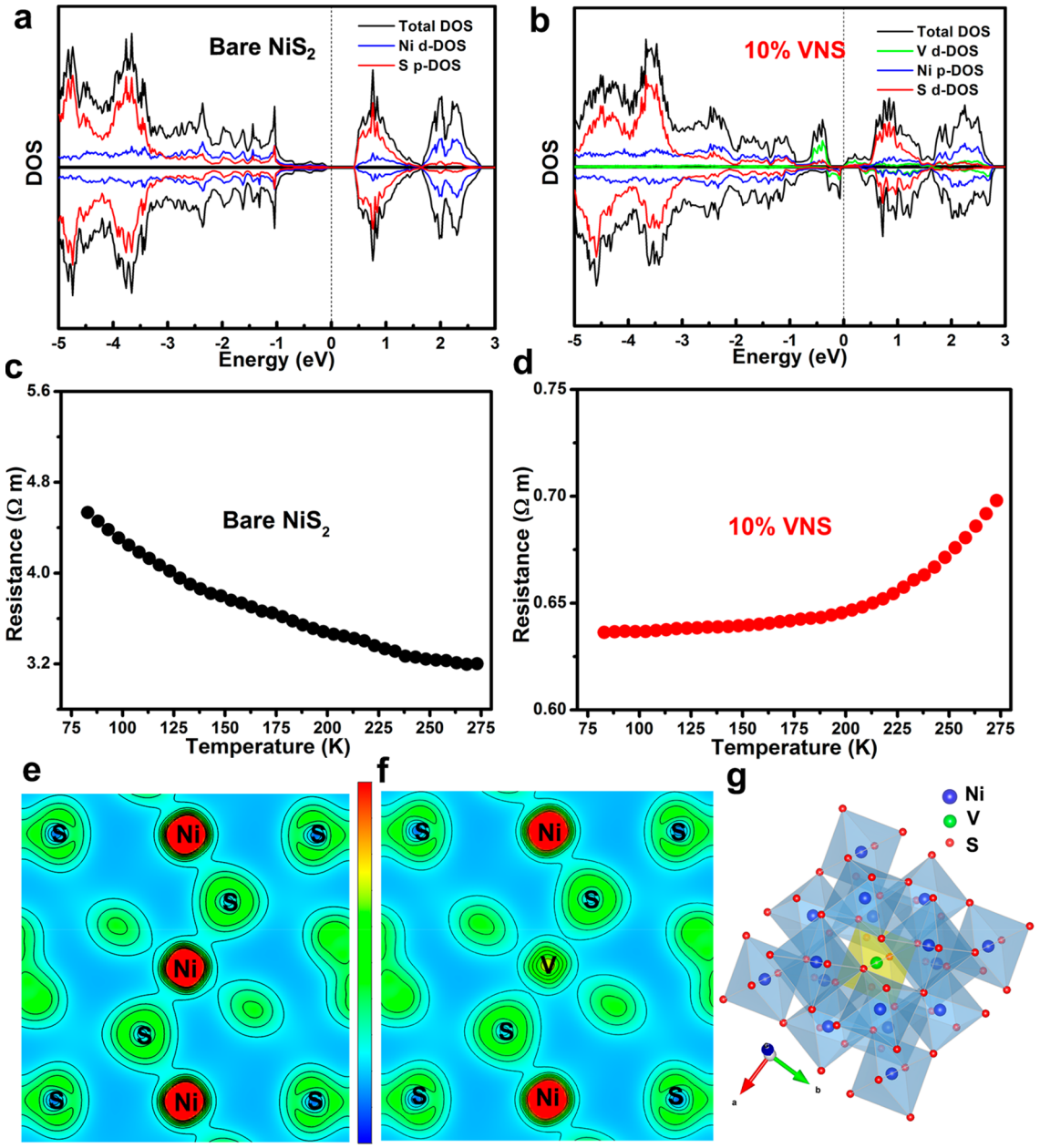

Figure 4. (a, b) Calculated DOS of bare NiS_2 (a) and 10% VNS (b). (c, d) Temperature-dependent resistivity of bare NiS_2 (c) and 10% VNS (d). (e, f) Charge-density contour map for bare NiS_2 (e) and 10% VNS (f). (g) Crystal structure of 10% VNS.

1c and S3 and S4) revealed that the 10% VNS sample always kept original nanosheets similarly to NiV LDH precursor (Figure S5). Further HRTEM (Figure 1d) showed two equal interplanar distances (2.00 Å) with a dihedral angle of about 90° corresponding to the (220) and (2$\bar{2}$0) lattice planes of the 10% VNS, further supporting crystal structure of typical pyrite NiS_2. The high-angle annular dark-field (HAADF) image and the corresponding energy dispersive X-ray (EDX) mapping of 10% VNS presented the uniform distribution of Ni, V, and S elements (Figure 1e). More importantly, it holds the key to a further in-depth exploring existing form of V within NiS_2 and the modulation of atomic and electronic structure, as discussed in the following sections.

The X-ray photoelectron spectroscopy (XPS) was performed to investigate the chemical states information on 10% VNS (Figure 2). The XPS survey (Figure S6) confirmed the coexistence of V, Ni, and S in 10% VNS compounds. Furthermore, the high-resolution XPS peaks of Ni 2p XPS core level (Figure 2a) showed that the two peaks located at about 856.3 eV and about 873.8 eV were assigned to the spin−orbit doublet of 2p orbital of Ni^{2+} (Ni^{2+} $2p_{3/2}$ and Ni^{2+} $2p_{1/2}$) along with two typical Ni^{2+} "shake up" satellites.[41−43] Two main peaks of V 2p (Figure 2b) located at 516.4 and 523.9 eV were recognized as V^{4+} $2p_{3/2}$ and V^{4+} $2p_{1/2}$, confirming the existence of V^{4+} in 10% VNS.[44−46] With respect to the S 2p spectrum in Figure 2c, the two strong peaks at about 162.5 and 163.7 eV were attributed as the S $2p_{3/2}$ and S $2p_{1/2}$.[47−49] The weak peak occurring at about 168.5 eV could be recognized as a S−O bond due to slight surface oxidization.[50] The XPS results were in good agreement with other previous reports,[51] suggesting the successful synthesis of nickel-based sulfide. Notably, compared to bare NiS_2 (XPS survey and high-

DOI: 10.1021/acsnano.7b06501
ACS Nano 2017, 11, 11574−11583

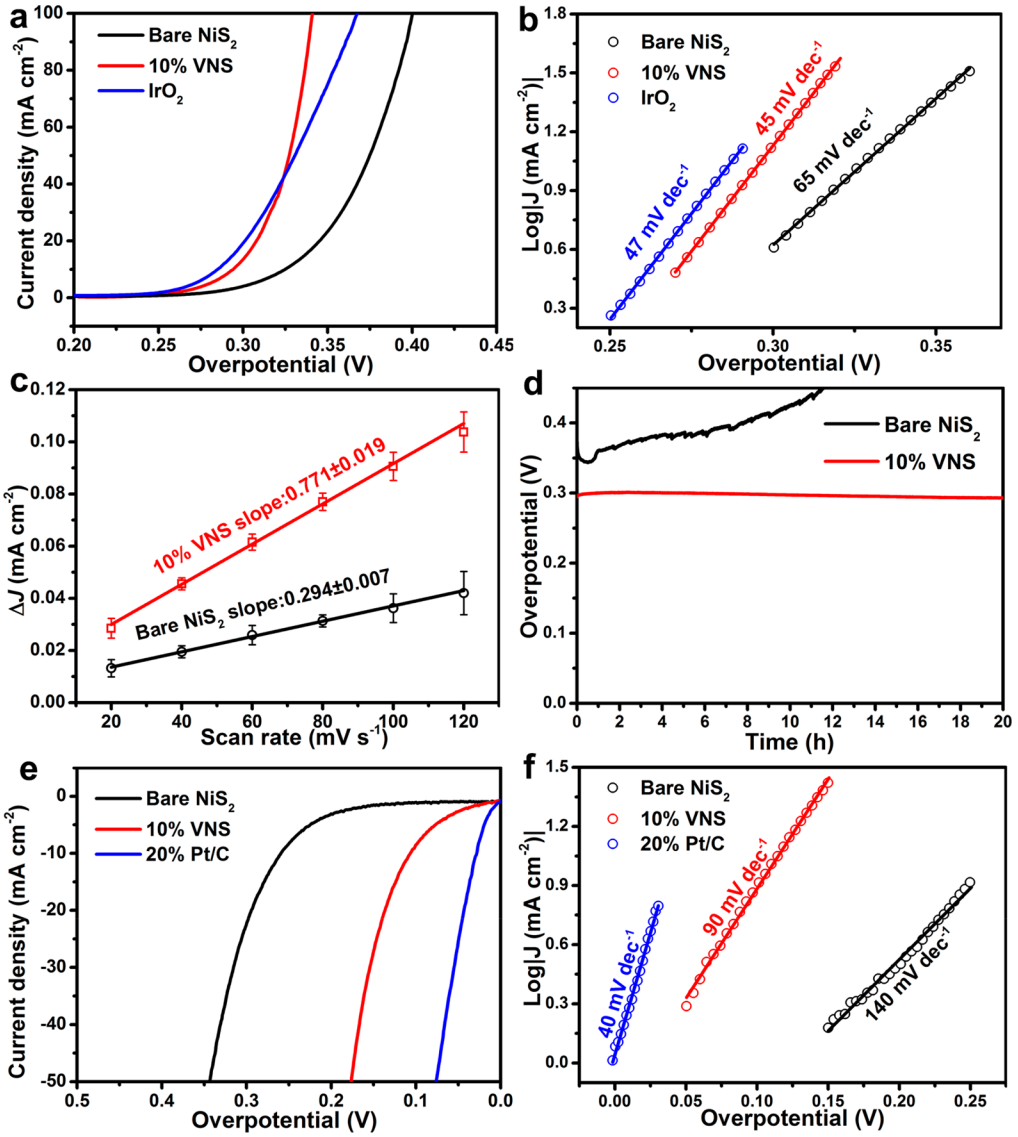

Figure 5. (a) LSV polarization curves of bare NiS_2, IrO_2, and 10% VNS for OER. (b) Corresponding Tafel plots of bare NiS_2, IrO_2, and 10% VNS. (c) Current difference of bare NiS_2, Pt/C, and 10% VNS against different scan rates for the estimation of double-layer capacitance; error bars mean standard deviation from three independent measurements. (d) Chronopotentiometry curves at a constant current density of 10 mA cm^{-2} of 10% VNS and bare NiS_2. (e) LSV polarization curves of bare NiS_2 and 10% VNS for HER. (f) Corresponding Tafel plots of bare NiS_2, Pt/C, and 10% VNS toward HER.

resolution S 2p XPS peaks of bare NiS_2 were shown in Figure S7 and S8), the binding energies had a noticeable downshift of about 0.5 eV in Ni 2p XPS pattern of 10% VNS (Figure 2d), revealing the increment of Ni chemical potentials in 10% VNS from V doping. Such an increment probably attributes to the electron transfer due to existence of V^{4+}, which will be further explored in the following section.

The good preservation of long-range order in 10% VNS was already confirmed in the above-mentioned results. In order to further understand the short-range order change of 10% VNS, an X-ray absorption fine structure (XAFS) measurement was conducted owing to its high sensitivity toward local structures. The Ni K-edge $k^3(\chi(k))$ oscillation functions of bare NiS_2 and 10% VNS were similar (Figure 3a), confirming the good maintenance of short-range order of NiS_2 with V incorporation. The corresponding Fourier transform (FT) curves showed a main peak at approximately 1.90 Å (Figure S9), which was recognized as a Ni−S correlation. However, for 10% VNS, the peak intensity was slightly decreased, implying the surface disorder of 10% VNS due to V incorporation. Ni K-edge X-ray absorption near-edge structures (XANES) region was further conducted to evaluate the electronic structure modulation by inducing V doping (Figure 3b). The spectral feature A (Figure 3b) without any energy shift between bare NiS_2 and 10% VNS confirmed that the NiS_2 structure was well preserved after V doping, according to previous XRD results and XAFS analysis. However, as exhibited in the inset of Figure 3b, the absorption threshold of 10% VNS shifted to a lower energy compared to that of bare NiS_2, revealing the reduction of Ni oxidation states in 10% VNS, in accordance with previous XPS results (Figure 2d). More importantly, the Ni L-edge XANES (Figure 3c) indicated a decrease of the unoccupied electron density states at Ni sites within 10% VNS, forcefully confirming a higher electron density of Ni sites.[52] Then, existing forms of V within doped NiS_2 were investigated by conducting the V K-edge XAFS measurement. FT $k^3(\chi(k))$ of VS_2 (Figure 3d) displayed

DOI: 10.1021/acsnano.7b06501
ACS Nano 2017, 11, 11574−11583

two peaks at about 1.84 and 2.69 Å, which could be recognized as V−S and V−V correlations, respectively. Impressively, 10% VNS displayed only one peak belonging to V−S correlation, and no V−V correlation was observed, implying the presence of isolated V heteroatoms located at Ni positions. In addition, the V−S peak for 10% VNS showed an upshift compared to that of VS_2, which further provided corroborative evidence of V existent forms in V-doped NiS_2 because of the longer bond length of Ni−S than that of V−S.

To better understand the electronic structure reconfiguration of NiS_2 with V incorporation in theory, the density of states (DOS) of bare NiS_2 and 10% VNS were calculated (Figure 4a). The calculated result indicated that the bare NiS_2 exhibited a typical semiconductor characteristic with a narrow bandgap of about 0.41 eV, which matched well with previous researches.[53] For 10% VNS, a definite zero band gap was achieved, indicating the metallic nature due to V doping into NiS_2 (Figure 4b). To further explore the electron transport behavior of bare NiS_2 and 10% VNS, the temperature-dependent resistivity was conducted. The electrical resistivity of bare NiS_2 decreased with the increasing temperature (Figure 4c), confirming the typical semiconductor characteristic. However, the electrical resistivity of 10% VNS increases with the raising temperature (Figure 4d), which conformed to the typical feature of metallic character. Furthermore, 10% VNS showed an obviously lower resistivity than bare NiS_2, and thus a faster electron transfer in 10% VNS would be realized. The charge density of V in 10% VNS (Figure 4f,g) distinctly decreased compared to that of Ni at the same site in bare NiS_2 (Figures 4e and S10). Moreover, a contour map showed that the charge density around V atoms was lower than that around Ni atoms, indicating the electron transfer from V atom to nearby atoms. Briefly, we successfully tuned the electronic structure of semiconductive pyrite NiS_2 to metallic 10% VNS *via* V incorporation.

In our case, to evaluate the electrocatalytic performance brought by electronic structure reconfiguration, electrochemical OER activities were measured in a standard test system (see Experimental Section for details). LSV curves (Figure 5a) indicated that 10% VNS exhibited superior OER catalytic performance relative to bare NiS_2 and even higher activity than IrO_2 above an overpotential of 330 mV. Additionally, the significantly lower overpotential (290 mV) at 10 mA cm^{-2} for 10% VNS than that (325 mV) for bare NiS_2 forcefully verified the advantage of metallic V-doped NiS_2 toward OER, which is comparable with other recently reported catalysts (Table S2). Moreover, to estimate the reaction kinetics of bare NiS_2 and 10% VNS, the Tafel slopes of these samples were further compared (Figure 5b). Clearly, linear fitting of Tafel plots showed a Tafel slope of about 45 mV dec^{-1} for 10% VNS, which is obviously smaller than that of bare NiS_2 (65 mV dec^{-1}). These results reveal the faster reaction kinetics of 10% VNS and strongly confirmed the excellent OER performance of optimized 10% VNS. Besides, the OER behavior was also evaluated by estimating the electrochemical active surface areas (ECSAs), which are proportionally positive to the double-layer capacitance (C_{dl}). The C_{dl} were determined by taking cyclic voltammetry (CV) at different scan rates (see Experimental Section for details). The C_{dl} value of 10% VNS was 0.771 mF cm^{-2} (Figure 5c), which is about 2.6 times that of the bare NiS_2 (0.294 mF cm^{-2}). Meanwhile, looking back at Figure 5a, at the same overpotential of 325 mV, the current density of 10% VNS (45 mA cm^{-2}) is more than 4-fold that of bare NiS_2 (10 mA cm^{-2}), indicating that the increase of active surface area is not the only reason for the impressing catalytic performance of 10% VNS. The intrinsic metallic character of 10% VNS probably brought improved electrocatalytic catalytic activity, in good agreement with previous work.[28−33] Long-term durability of OER was further investigated owing to its important role in practical applications. The durability tests were conducted using a chronopotentiometry method at a constant current density of 10 mA cm^{-2} (Figure 5d). The excellent long-term durability made it a potential candidate for practical applications. To completely evaluate the electrochemical performance of 10% VNS, 5% VNS and 25% VNS were further synthesized, characterized, and compared (Figures S11−S17). The optimized OER performance of 10% VNS might originate from the largest ECSA among these V-doped NiS_2 with different ratios. Moreover, a proper element doping ratio could improve the intrinsic activity by tuning the reaction free energy of the reaction rate-determining step for OER,[40,54] which might be another reason for the best OER activity of 10% VNS.

The HER catalytic activity of the 10% VNS was also studied in N_2-saturated 1 M KOH (see Experimental Section for details). Impressive catalytic performance was found for 10% VNS (Figure 5e). The overpotential for 10% VNS to reach a current density of 10 mA cm^{-2} was 110 mV, which is much lower than that of bare NiS_2 (260 mV). The 10% VNS candidate always showed competitive HER catalytic performance with other recently reported high active overall water splitting catalysts (Table S3). The Tafel slope of 10% VNS was 90 mV dec^{-1}, which is better than that of bare NiS_2 (140 mV dec^{-1}), indicating the favorable reaction kinetic of 10% VNS (Figure 5f). Chronopotentiometry method with a constant current density of 10 mA cm^{-2} was further employed to evaluate the long-term stability of 10% VNS and bare NiS_2 for comparison. As a result, 10% VNS maintained the electrochemical catalytic HER activity even after 20 h (Figure S18), which confirms the good stability of 10% VNS. The electrocatalytic HER performance of 10% VNS, 5% VNS, and 25% VNS were also characterized and compared (Figures S19−S21). The preferable HER activity of 10% VNS might attribute to an appropriate doping content which could tune Gibbs free energies of hydrogen adsorption.[55] Further research into the precise reaction mechanism is under way.

Based on the superior electrochemical OER and HER performance of the 10% VNS, a two-electrode system electrolyzer with nickel foam supported 10% VNS as both the cathode and anode was assembled to confirm the catalytic performance in practical applications. O_2-saturated 1 M KOH was used as the electrolyte, and the catalytic performances of nickel foam‖nickel foam as well as Pt/C‖IrO_2 were also tested for comparison. Optical photograph (Figure 6a) showed the generation of hydrogen and oxygen bubbles from overall water splitting. LSV polarization curve of the 10% VNS showed good overall water splitting performance and was comparable to that of Pt/C‖IrO_2. 10% VNS required a total cell voltage of 1.56 V for achieving a current density of 10 mA cm^{-2}, which is slightly better than that of Pt/C‖IrO_2 (1.57 V). 10% VNS showed comparable overall water splitting performance to recently reported catalysts (Table S4). What's more, Figure 6c showed that the 10% VNS exhibits excellent long-term durability for at least a 20 h test. Schematic diagram of water splitting of 10% VNS (Figure 6d) showed bifunctional catalytic feature and fast electron transfer brought by metallic characteristics.

DOI: 10.1021/acsnano.7b06501
ACS Nano 2017, 11, 11574−11583

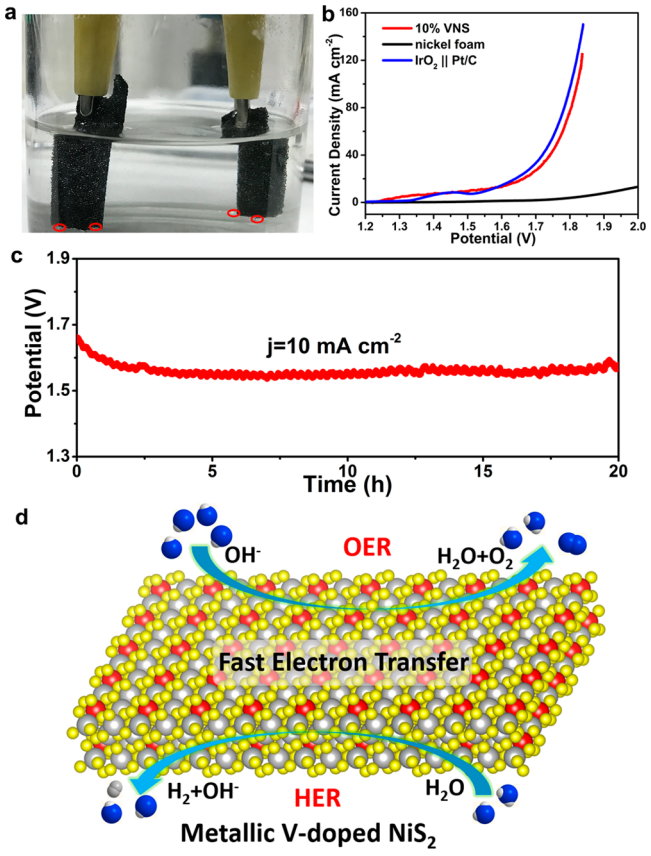

Figure 6. (a) Optical photograph showing the generation of hydrogen and oxygen bubbles from overall water splitting on nickel foam supported 10% VNS as both the anode and cathode in a typical two-electrode system. (b) LSV curves of the typical two-electrode system by using nickel foam supported 10% VNS as both the cathode and anode in 1 M KOH, bare nickel foam, and nickel foam supported IrO_2||Pt/C were tested for comparison. (c) Chrono-potentiometry curves at a constant current density of 10 mA cm^{-2} of 10% VNS for overall water splitting test. (d) Schematic diagram of the overall water splitting of 10% VNS.

CONCLUSION

In summary, we have provided the demonstration of electronic structure reconfiguration of pyrite NiS_2 from typical semiconductive characteristics to metallic characteristics *via* atomic V replacement. The semiconductor-metal transition was confirmed *via* elaborate experiment investigations and DFT calculations. Notably, our advanced XAS measurements revealed that electronic structure reconfiguration of NiS_2 originated from the electron transfer between doped V heteroatoms and Ni sites. As a proof-of-concept outcome, a total cell voltage of 1.56 V was required for metallic V-doped NiS_2 to achieve a current density of 10 mA cm^{-2} in overall water splitting, making it a potential candidate to be one of the best nickel-based overall water splitting catalysts. Furthermore, our research reveals that semiconductor-metal transitions might be a particularly effective strategy to optimize the electrochemically catalytic performance.

EXPERIMENTAL SECTION

Synthesis of Nickel and NiV Layered Double Hydroxides. NiV LDHs were synthesized by a hydrothermal method as reported previously with some small modifications.[38] Typically, for $Ni_{0.9}V_{0.1}$ LDH, $NiCl_2{\cdot}6H_2O$ (2.70 mmol) and VCl_3 (0.30 mmol) were dissolved in deionized water (80 mL) under full stirring, followed by the addition of urea (5 mmol). After stirring for at least 30 min, the above solution was transferred to a 100 mL Teflon-lined stainless steel autoclave at 120 °C for 12 h. The products were centrifuged and washed with deionized water and ethanol for several times. Finally, the samples were undertaken by freeze-drying and then collected. NiV LDH with different ratios of Ni and V was synthesized by following the same processes except adding different mole ratios of $NiCl_2{\cdot}6H_2O$ and VCl_3, and the total amount of Ni and V was kept to 3.00 mmol. $Ni(OH)_2$ was synthesized without adding VCl_3 to the preparation.

Synthesis of VNS with Different Doping Ratios. The $Ni(OH)_2$ and NiV LDHs were sulfidized to bare NiS_2 and V-doped NiS_2 by a modified procedure as reported previously.[56] Briefly, taking 10% VNS for example, 20 mg of $Ni_{0.9}V_{0.1}$ LDH was fully ground with 100 mg of sulfur powder by an agate mortar. The mixture was paved in an aluminum oxide flat bottom boat, and then this boat was placed in the center of a quartz tube. Another aluminum oxide boat containing 1 g of sulfur powder was placed in the same quartz tube at the farthest upstream position in the heating area. The furnace was heated to 400 °C with a heating rate of 2 °C min^{-1} under a constant flow of H_2/Ar (5% H_2) carrier gas at 50 sccm for 200 min. After naturally cooling down to room temperature, the product was then washed and centrifuged with ethanol and CS_2 for several times and then dried at 60 °C overnight. VS_2 bulk for XAFS comparison was synthesized according to previous research.[57] In brief, $LiVS_2$ was synthesized by solid reacting Li_2CO_3 with V_2O_5 under H_2S atmosphere. After washing $LiVS_2$ with iodine solution for several times, the final product was vacuum-dried at 60 °C for 6 h.

Materials Characterization. Power X-ray diffraction (PXRD) patterns were carried out with a Philips X'Pert Pro Super diffractometer with Cu Kα radiation (λ = 1.54 Å). The morphology and microstructures were observed by a JEOL JSM-6700F field emission scanning electron microscopy (SEM) and a JEM-2100F field emission transmission electron microscopy (TEM) with an acceleration voltage of 200 kV. The energy-dispersive X-ray spectroscopy (EDX) elemental mapping characterizations were also taken with JEM-2100F field emission transmission. X-ray photoelectron spectroscopy (XPS) was conducted on a Thermo ESCALAB 250 X-ray photoelectron spectrometer with a Mg source (Kα = 1253.6 eV). The binding energies were calibrated by using the C 1s level at the energy of 284.5 eV as a reference. X-ray absorption fine structure (XAFS) measurements at the Ni K-edge were performed in transmission mode at the BL14W of the Shanghai Synchrotron Radiation Facility (SSRF). XAFS measurements at the V K-edge were performed at Beijing Synchrotron Radiation Facility (SSRF). The Ni L-edge X-ray absorption near edge structures (XANES) were performed in BL12B-α of the Hefei National Synchrotron Radiation Laboratory (NSRL). XAFS data were analyzed with the ATHENA and ARTEMIS code of Ravel. The absorption curves were normalized to 1, and the EXAFS signals $\chi(k)$ were obtained after the removal of the pre-edge and post-edge background. The Fourier transform (FT) spectra were obtained as $k^3\chi(k)$ with a Hanning window in the range 3−12 $Å^{-1}$.

Electrochemical Measurements. All electrochemical measurements were carried out on a conventional three-electrode system with an electrochemical workstation (CHI 760E). For the OER and HER tests, a Ag/AgCl (saturated KCl) electrode was used as the reference electrode, and a graphite rod was used as the counter electrode. Four mg of the samples and 40 μL 5% Nafion solution were put in 1 mL mixture of water/isopropanol with volume ratio of 3:1 and dispersed by ultrasonication for at least 60 min to form a homogeneous ink. After that, 5 μL of this ink was carefully dropped onto a glassy carbon electrode (GCE) with a diameter of 3 mm and dried in air atmosphere to form a catalyst mass loading of about 0.272 mg cm^{-2}. The potentials were converted to reversible hydrogen electrode (RHE) by using $E_{RHE} = E_{Ag/AgCl} + 0.059\ pH + 0.197$ V, and overpotential for OER was $\eta = E_{RHE} - 1.23\ V = E_{Ag/AgCl} - 0.207$ V. The polarization curves were recorded with a scan rate of 5 mV s^{-1} in N_2/O_2-saturated 1 M KOH (purged with pure N_2/O_2 for at least 60 min, N_2 for HER and O_2 for OER) with a 90% IR compensation. The double-layer capacitance (C_{dl}) was determined by taking cyclic voltammetry in the potential

DOI: 10.1021/acsnano.7b06501
ACS Nano 2017, 11, 11574−11583

windows 0.1−0.25 V *versus* Ag/AgCl under different scan rates ranging from 20 to 120 mV s^{-1}. By plotting $\Delta j = (j_a - j_c)$ at 0.18 V *versus* Ag/AgCl reference electrode against the scan rate, the linear slope is twice the double-layer capacitance C_{dl}. For overall water splitting test, nickel foam was first washed with HCl, ethanol, and acetone for several times and then dried. The above mixture was coated onto a piece of the cleaned nickel foam and dried overnight in air to evaporate solvent and yielded a catalyst mass loading of about 1 mg cm^{-2}. The polarization curves of overall water splitting were recorded with a scan rate of 5 mV s^{-1} in O_2-saturated 1 M KOH with a 90% IR compensation.

DFT Calculation. All calculations were performed using the Vienna *ab Initio* Simulation Package (VASP).[58,59] The generalized gradient approximation (GGA) in the form of the Perdew−Burke−Ernzerhof (PBE) exchange model was used in the description of the exchange−correlation potential.[60,61] A plane-wave basis set with an energy cutoff of 500 eV was used. The Brillouin zone was sampled in a 5 × 5 × 9 mesh. Calculations of pure and 10% VNS were carried out with 2 × 1 × 1 supercells to achieve the appropriate doping concentration. 3d electrons of Ni were treated using the GGA+*U* method, where the onsite Coulomb repulsion (Hubbard *U*) and the atomic orbital intraexchange (Hund's parameter *J*) are simplified to U_{eff} using this equation: $U_{eff} = U - J$. A value of 4.5 eV for the U_{eff} was used because the calculated band gap (0.41 eV) of NiS_2 was very close to the experimental data by using this value.[50] Ionic relaxations were conducted until all force components became <0.01 eV A^{-1}.

ASSOCIATED CONTENT

Supporting Information

The Supporting Information is available free of charge on the ACS Publications website at DOI: 10.1021/acsnano.7b06501.

Additional Schematic diagram, SEM images, TEM images, XPS spectrum, XAFS analysis, XRD patterns, ICP results and electrochemical characterizations (PDF)

AUTHOR INFORMATION

Corresponding Authors

*E-mail: jhlworld@ustc.edu.cn.
*E-mail: song2012@ustc.edu.cn.

ORCID

Li Song: 0000-0003-0585-8519

Author Contributions

L.S. and H.J. planned the project. H.L. carried out most of the sample preparation and material measurement. Q.H. performed DFT calculations. Y.L. and C.S. conducted XAS experiments and data analysis. Y.Z. and M.H. carried out soft XAS experiments and data analysis. All authors discussed the results and participated in writing the manuscript.

Notes

The authors declare no competing financial interest.

ACKNOWLEDGMENTS

This work is financially supported by MOST (2017YFA0303500, 2014CB848900), NSFC (U1532112, 11375198, 11574280, 11605201, 21706248), CAS Key Research Program of Frontier Sciences (QYZDB-SSW-SLH018), and CAS Iterdisciplinary Innovation Team. L.S. acknowledges the recruitment program of global experts, the CAS Hundred Talent Program and Key Laboratory of Advanced Energy Materials Chemistry (Ministry of Education) Nankai University. We thank the Shanghai synchrotron Radiation Facility (14W1, SSRF), the Beijing Synchrotron Radiation Facility (1W1B and soft-X-ray endstation, BSRF), the Hefei Synchrotron Radiation Facility (Photoemission, MCD and Catalysis/Surface Science Endstations, NSRL), and the USTC Center for Micro and Nanoscale Research and Fabrication for helps in characterizations.

REFERENCES

(1) Dresselhaus, M. S.; Thomas, I. L. Alternative Energy Technologies. *Nature* **2001**, *414*, 332−337.
(2) Arico, A. S.; Bruce, P.; Scrosati, B.; Tarascon, J. M.; Van Schalkwijk, W. Nanostructured Materials for Advanced Energy Conversion and Storage Devices. *Nat. Mater.* **2005**, *4*, 366−377.
(3) Schlapbach, L.; Zuttel, A. Hydrogen-Storage Materials for Mobile Applications. *Nature* **2001**, *414*, 353−358.
(4) Cook, T. R.; Dogutan, D. K.; Reece, S. Y.; Surendranath, Y.; Teets, T. S.; Nocera, D. G. Solar Energy Supply and Storage for the Legacy and Non Legacy Worlds. *Chem. Rev.* **2010**, *110*, 6474−6502.
(5) McKone, J. R.; Lewis, N. S.; Gray, H. B. Will Solar-Driven Water-Splitting Devices See the Light of Day? *Chem. Mater.* **2014**, *26*, 407−414.
(6) Zou, X. X.; Zhang, Y. Noble Metal-Free Hydrogen Evolution Catalysts for Water Splitting. *Chem. Soc. Rev.* **2015**, *44*, 5148−5180.
(7) Jia, Y.; Zhang, L.; Du, A.; Gao, G.; Chen, J.; Yan, X.; Brown, C. L.; Yao, X. Defect Graphene as a Trifunctional Catalyst for Electrochemical Reactions. *Adv. Mater.* **2016**, *28*, 9532−9538.
(8) Petrykin, V.; Macounova, K.; Shlyakhtin, O. A.; Krtil, P. Tailoring The Selectivity for Electrocatalytic Oxygen Evolution on Ruthenium Oxides by Zinc Substitution. *Angew. Chem., Int. Ed.* **2010**, *49*, 4813−4815.
(9) Lee, Y.; Suntivich, J.; May, K. J.; Perry, E. E.; Shao-Horn, Y. Synthesis and Activities of Rutile IrO_2 and RuO_2 Nanoparticles for Oxygen Evolution in Acid and Alkaline Solutions. *J. Phys. Chem. Lett.* **2012**, *3*, 399−404.
(10) Esposito, D. V.; Hunt, S. T.; Stottlemyer, A. L.; Dobson, K. D.; McCandless, B. E.; Birkmire, R. W.; Chen, J. G. G. Low-Cost Hydrogen-Evolution Catalysts Based on Monolayer Platinum on Tungsten Monocarbide Substrates. *Angew. Chem., Int. Ed.* **2010**, *49*, 9859−9862.
(11) Vesborg, P. C. K.; Jaramillo, T. F. Addressing the Terawatt Challenge: Scalability in the Supply of Chemical Elements for Renewable Energy. *RSC Adv.* **2012**, *2*, 7933−7947.
(12) Zhao, L.; Dong, B.; Li, S.; Zhou, L.; Lai, L.; Wang, Z.; Zhao, S.; Han, M.; Gao, K.; Lu, M.; et al. Inter-Diffusion Reaction Assisted Hybridization of Two-dimensional Metal-Organic Frameworks and $Ti_3C_2T_x$ Nanosheets for Electrocatalytic Oxygen Evolution. *ACS Nano* **2017**, *11*, 5800−5807.
(13) Ma, N.; Jia, Y.; Yang, X. F.; She, X. L.; Zhang, L. Z.; Peng, Z.; Yao, X. D.; Yang, D. J. Seaweed Biomass Derived (Ni,Co)/CNT Nanoaerogels: Efficient Bifunctional Electrocatalysts for Oxygen Evolution and Reduction Reactions. *J. Mater. Chem. A* **2016**, *4*, 6376−6384.
(14) Li, J.; Wang, Y.; Zhou, T.; Zhang, H.; Sun, X.; Tang, J.; Zhang, L.; Al-Enizi, A. M.; Yang, Z.; Zheng, G. Nanoparticle Superlattices as Efficient Bifunctional Electrocatalysts for Water Splitting. *J. Am. Chem. Soc.* **2015**, *137*, 14305−14312.
(15) Tan, Y.; Wang, H.; Liu, P.; Cheng, C.; Zhu, F.; Hirata, A.; Chen, M. 3D Nanoporous Metal Phosphides toward High-Efficiency Electrochemical Hydrogen Production. *Adv. Mater.* **2016**, *28*, 2951−2955.
(16) Zhu, Y.; Zhou, W.; Zhong, Y.; Bu, Y.; Chen, X.; Zhong, Q.; Liu, M.; Shao, Z. A Perovskite Nanorod as Bifunctional Electrocatalyst for Overall Water Splitting. *Adv. Energy Mater.* **2017**, *7*, 1602122.
(17) Shi, Y.; Zhang, B. Recent Advances in Transition Metal Phosphide Nanomaterials: Synthesis and Applications in Hydrogen Evolution Reaction. *Chem. Soc. Rev.* **2016**, *45*, 1529−1541.
(18) Zhuang, L. H.; Ge, L.; Yang, Y. S.; Li, M. R.; Jia, Y.; Yao, X. D.; Zhu, Z. H. Ultrathin Iron-Cobalt Oxide Nanosheets with Abundant Oxygen Vacancies for the Oxygen Evolution Reaction. *Adv. Mater.* **2017**, *29*, 1606793.
(19) Yang, K.; Wang, X.; Li, H.; Chen, B.; Zhang, X.; Li, S.; Wang, N.; Zhang, H.; Huang, X.; Huang, W. Composition-and Phase-Controlled Synthesis and Applications of Alloyed Phase Hetero-

DOI: 10.1021/acsnano.7b06501
ACS Nano 2017, 11, 11574−11583

structures of Transition Metal Disulphides. *Nanoscale* **2017**, *9*, 5102−5109.
(20) Ikeshoji, T.; Otani, M.; Hamada, I.; Okamoto, Y. Reversible Redox Reaction and Water Configuration on a Positively Charged Platinum Surface: First Principles Molecular Dynamics Simulation. *Phys. Chem. Chem. Phys.* **2011**, *13*, 20223−20227.
(21) Rossmeisl, J.; Qu, Z.-W.; Zhu, H.; Kroes, G.-J.; Nørskov, J. K. Electrolysis of Water on Oxide Surfaces. *J. Electroanal. Chem.* **2007**, *607*, 83−89.
(22) Koper, M. T. Thermodynamic Theory of Multi-Electron Transfer Reactions: Implications for Electrocatalysis. *J. Electroanal. Chem.* **2011**, *660*, 254−260.
(23) Qu, K.; Zheng, Y.; Jiao, Y.; Zhang, X.; Dai, S.; Qiao, S. Z. Polydopamine-Inspired, Dual Heteroatom Doped Carbon Nanotubes for Highly Efficient Overall Water Splitting. *Adv. Energy Mater.* **2017**, *7*, 1602068.
(24) Yue, X.; Huang, S.; Cai, J.; Jin, Y.; Shen, P. K. Heteroatoms Dual Doped Porous Graphene Nanosheets as Efficient Bifunctional Metal-free Electrocatalysts for Overall Water-Splitting. *J. Mater. Chem. A* **2017**, *5*, 7784−7790.
(25) Yoon, T.; Kim, K. S. One-Step Synthesis of CoS-Doped β-$Co(OH)_2$@Amorphous MoS_{2+x} Hybrid Catalyst Grown on Nickel Foam for High-Performance Electrochemical Overall Water Splitting. *Adv. Funct. Mater.* **2016**, *26*, 7386−7393.
(26) Xue, Z. H.; Su, H.; Yu, Q. Y.; Zhang, B.; Wang, H. H.; Li, X. H.; Chen, J. S. Janus Co/CoP Nanoparticles as Efficient Mott−Schottky Electrocatalysts for Overall Water Splitting in Wide pH Range. *Adv. Energy Mater.* **2017**, *7*, 1602355.
(27) Yan, X.; Jia, Y.; Chen, J.; Zhu, Z.; Yao, X. Defective-Activated-Carbon-Supported Mn-Co Nanoparticles as a Highly Efficient Electrocatalyst for Oxygen Reduction. *Adv. Mater.* **2016**, *28*, 8771−8778.
(28) Liu, Q.; Fang, Q.; Chu, W.; Wan, Y.; Li, X.; Xu, W.; Habib, M.; Tao, S.; Zhou, Y.; Liu, D.; et al. Electron-Doped 1T-MoS_2 *via* Interface Engineering for Enhanced Electrocatalytic Hydrogen Evolution. *Chem. Mater.* **2017**, *29*, 4738−4744.
(29) Li, H.; Chen, S.; Jia, X.; Xu, B.; Lin, H.; Yang, H.; Song, L.; Wang, X. Amorphous Nickel-Cobalt Complexes Hybridized with 1T-phase Molybdenum Disulfide *via* Hydrazine-Induced Phase Transformation for Water Splitting. *Nat. Commun.* **2017**, *8*, 15377.
(30) Xu, K.; Chen, P.; Li, X.; Tong, Y.; Ding, H.; Wu, X.; Chu, W.; Peng, Z.; Wu, C.; Xie, Y. Metallic Nickel Nitride Nanosheets Realizing Enhanced Electrochemical Water Oxidation. *J. Am. Chem. Soc.* **2015**, *137*, 4119−4125.
(31) Stern, L.-A.; Feng, L.; Song, F.; Hu, X. Ni_2P as a Janus Catalyst for Water Splitting: the Oxygen Evolution Activity of Ni_2P Nanoparticles. *Energy Environ. Sci.* **2015**, *8*, 2347−2351.
(32) Feng, L.; Vrubel, H.; Bensimon, M.; Hu, X. Easily-prepared Dinickel Phosphide (Ni_2P) Nanoparticles as an Efficient and Robust Electrocatalyst for Hydrogen Evolution. *Phys. Chem. Chem. Phys.* **2014**, *16*, 5917−5921.
(33) Pu, Z.; Liu, Q.; Tang, C.; Asiri, A. M.; Sun, X. Ni_2P Nanoparticle Films Supported on a Ti Plate as an Efficient Hydrogen Evolution Cathode. *Nanoscale* **2014**, *6*, 11031−11034.
(34) Feng, L.-L.; Yu, G.; Wu, Y.; Li, G.-D.; Li, H.; Sun, Y.; Asefa, T.; Chen, W.; Zou, X. High-Index Faceted Ni_3S_2 Nanosheet Arrays as Highly Active and Ultrastable Electrocatalysts for Water Splitting. *J. Am. Chem. Soc.* **2015**, *137*, 14023−14026.
(35) Zhou, W.; Wu, X.-J.; Cao, X.; Huang, X.; Tan, C.; Tian, J.; Liu, H.; Wang, J.; Zhang, H. Ni_3S_2 Nanorods/Ni Foam Composite Electrode with Low Overpotential for Electrocatalytic Oxygen Evolution. *Energy Environ. Sci.* **2013**, *6*, 2921−2924.
(36) Sun, X.; Dai, J.; Guo, Y.; Wu, C.; Hu, F.; Zhao, J.; Zeng, X.; Xie, Y. Semimetallic Molybdenum Disulfide Ultrathin Nanosheets as an Efficient Electrocatalyst for Hydrogen Evolution. *Nanoscale* **2014**, *6*, 8359−8367.
(37) Lei, F.; Zhang, L.; Sun, Y.; Liang, L.; Liu, K.; Xu, J.; Zhang, Q.; Pan, B.; Luo, Y.; Xie, Y. Atomic-Layer-Confined Doping for Atomic-Level Insights into Visible-Light Water Splitting. *Angew. Chem., Int. Ed.* **2015**, *54*, 9266−9270.
(38) Cavani, F.; Trifirò, F.; Vaccari, A. Hydrotalcite-Type Anionic Clays: Preparation, Properties and Applications. *Catal. Today* **1991**, *11*, 173−301.
(39) Wang, Q.; O'Hare, D. Recent Advances in the Synthesis and Application of Layered Double Hydroxide (LDH) Nanosheets. *Chem. Rev.* **2012**, *112*, 4124−4155.
(40) Fan, K.; Chen, H.; Ji, Y.; Huang, H.; Claesson, P. M.; Daniel, Q.; Philippe, B.; Rensmo, H.; Li, F.; Luo, Y.; et al. Nickel-Vanadium Monolayer Double Hydroxide for Efficient Electrochemical Water Oxidation. *Nat. Commun.* **2016**, *7*, 11981.
(41) Peck, M. A.; Langell, M. A. Comparison of Nanoscaled and Bulk NiO Structural and Environmental Characteristics by XRD, XAFS, and XPS. *Chem. Mater.* **2012**, *24*, 4483−4490.
(42) Mansour, A. N. Characterization of NiO by XPS. *Surf. Sci. Spectra* **1994**, *3*, 231−238.
(43) Yuan, W.-J.; Li, J.-C.; Chen, P.; Shen, Y.-H.; Xie, A.-J. A One-Pot Hydrothermal Synthesis of 3D Nitrogen-Doped Graphene Aerogels-Supported NiS_2 Nanoparticles as Efficient Electrocatalysts for the Oxygen-Reduction Reaction. *J. Nanopart. Res.* **2014**, *16*, 2311.
(44) Silversmit, G.; Depla, D.; Poelman, H.; Marin, G. B.; De Gryse, R. Determination of the V2p XPS Binding Energies for Different Vanadium Oxidation States (V^{5+} to V^{0+}). *J. Electron Spectrosc. Relat. Phenom.* **2004**, *135*, 167−175.
(45) Demeter, M.; Neumann, M.; Reichelt, W. Mixed-Valence Vanadium Oxides Studied by XPS. *Surf. Sci.* **2000**, *454*, 41−44.
(46) Liang, H.; Shi, H.; Zhang, D.; Ming, F.; Wang, R.; Zhuo, J.; Wang, Z. Solution Growth of Vertical VS_2 Nanoplate Arrays for Electrocatalytic Hydrogen Evolution. *Chem. Mater.* **2016**, *28*, 5587−5591.
(47) Zhu, L.; Susac, D.; Teo, M.; Wong, K.; Wong, P.; Parsons, R.; Bizzotto, D.; Mitchell, K.; Campbell, S. Investigation of CoS_2-Based Thin Films as Model Catalysts for the Oxygen Reduction Reaction. *J. Catal.* **2008**, *258*, 235−242.
(48) Lichtman, D.; Craig, J. H.; Sailer, V.; Drinkwine, M. AES and XPS Spectra of Sulfur in Sulfur-Compounds. *Appl. Surf. Sci.* **1981**, *7*, 325−331.
(49) Leiro, J. A.; Mattila, S. S.; Laajalehto, K. XPS Study of the Sulphur 2p Spectra of Pyrite. *Surf. Sci.* **2003**, *547*, 157−161.
(50) Sun, H.; Qin, D.; Huang, S.; Guo, X.; Li, D.; Luo, Y.; Meng, Q. Dye-Sensitized Solar Cells with NiS Counter Electrodes Electrodeposited by a Potential Reversal Technique. *Energy Environ. Sci.* **2011**, *4*, 2630−2637.
(51) Yan, J.; Wu, H.; Chen, H.; Jiang, R.; Liu, S. F. Fe (III) Doped NiS_2 Nanosheet: A Highly Efficient and Low-Cost Hydrogen Evolution Catalyst. *J. Mater. Chem. A* **2017**, *5*, 10173−10181.
(52) Liang, Y. Y.; Li, Y. G.; Wang, H. L.; Zhou, J. G.; Wang, J.; Regier, T.; Dai, H. J. Co_3O_4 Nanocrystals on Graphene as a Synergistic Catalyst for Oxygen Reduction Reaction. *Nat. Mater.* **2011**, *10*, 780−786.
(53) Kautz, R. L.; Dresselhaus, M. S.; Adler, D.; Linz, A. Electrical and Optical Properties of NiS_2. *Phys. Rev. B* **1972**, *6*, 2078−2082.
(54) Liao, P.; Keith, J. A.; Carter, E. A. Water Oxidation on Pure and Doped hematite (0001) Surfaces: Prediction of Co and Ni as Effective Dopants for Electrocatalysis. *J. Am. Chem. Soc.* **2012**, *134*, 13296−13309.
(55) Greeley, J.; Jaramillo, T. F.; Bonde, J.; Chorkendorff, I.; Nørskov, J. K. Computational High-Throughput Screening of Electrocatalytic Materials for Hydrogen Evolution. *Nat. Mater.* **2006**, *5*, 909−913.
(56) Tang, C.; Pu, Z.; Liu, Q.; Asiri, A. M.; Sun, X. NiS_2 Nanosheets Array Grown on Carbon Cloth as an Efficient 3D Hydrogen Evolution Cathode. *Electrochim. Acta* **2015**, *153*, 508−514.
(57) Feng, J.; Peng, L.; Wu, C.; Sun, X.; Hu, S.; Lin, C.; Dai, J.; Yang, J.; Xie, Y. Giant Moisture Responsiveness of VS_2 Ultrathin Nanosheets for Novel Touchless Positioning Interface. *Adv. Mater.* **2012**, *24*, 1969−1974.

DOI: 10.1021/acsnano.7b06501
ACS Nano 2017, 11, 11574−11583

(58) Kresse, G.; Furthmüller, J. Efficient Iterative Schemes for *ab Initio* Total-Energy Calculations Using a Plane-Wave Basis Set. *Phys. Rev. B: Condens. Matter Mater. Phys.* **1996**, *54*, 11169.
(59) Kresse, G.; Furthmüller, J. Efficiency of *ab-Initio* Total Energy Calculations for Metals and Semiconductors Using a Plane-Wave Basis set. *Comput. Mater. Sci.* **1996**, *6*, 15−50.
(60) Perdew, J. P.; Chevary, J. A.; Vosko, S. H.; Jackson, K. A.; Pederson, M. R.; Singh, D. J.; Fiolhais, C. Atoms, Molecules, Solids, and Surfaces: Applications of the Generalized Gradient Approximation for Exchange and Correlation. *Phys. Rev. B: Condens. Matter Mater. Phys.* **1992**, *46*, 6671.
(61) Perdew, J. P.; Burke, K.; Ernzerhof, M. Generalized Gradient Approximation Made Simple. *Phys. Rev. Lett.* **1996**, *77*, 3865.

DOI: 10.1021/acsnano.7b06501
ACS Nano 2017, 11, 11574−11583